Acoustics of laminar boundary layer breakdown

By Meng Wang

1. Motivation and objectives

Boundary layer flow transition has long been suggested as a potential noise source in both marine (sonar-dome self noise) and aeronautical (aircraft cabin noise) applications, owing to the highly transient nature of the process (Farabee *et al.* 1989). The design of effective noise control strategies relies upon a clear understanding of the source mechanisms associated with the unsteady flow dynamics during transition. Due to formidable mathematical difficulties, theoretical predictions either are limited to early linear and weakly nonlinear stages of transition (Haj-Hariri & Akylas 1986; Akylas & Toplosky 1986), or employ acoustic analogy theories based on approximate source field data, often in the form of empirical correlation.

In the present work, an approach which combines direct numerical simulation of the source field with the Lighthill acoustic analogy (Lighthill 1952) is utilized. This approach takes advantage of the recent advancement in computational capabilities to obtain detailed information about the flow-induced acoustic sources. The transitional boundary layer flow is computed by solving the incompressible Navier-Stokes equations without model assumptions, thus allowing a direct evaluation of the pseudosound as well as source functions, including the Lighthill stress tensor and the wall shear stress. The latter are used for calculating the radiated pressure field based on the Curle-Powell solution (Curle 1955; Powell 1960) of the Lighthill equation. This procedure allows a quantitative assessment of noise source mechanisms and the associated radiation characteristics during transition from primary instability up to the laminar breakdown stage. In particular, one is interested in comparing the roles played by the fluctuating volume Reynolds stresses and the wall-shear-stresses, and in identifying specific flow processes and structures that are effective noise generators.

Natural transition in a boundary layer starts with modulated Tollmien-Schlichting (T-S) wave trains initiated by random excitations from free-stream turbulence (Gaster 1993). The laminar breakdown process which destroys the smooth, orderly flow pattern is a localized event triggered by instability mechanisms (Kachanov 1994). These observations suggest that without loss of generality, one could simulate the transition phenomena by following the evolution of a T-S wave packet instead of a periodic wave series as in controlled experiments. This results in considerable savings in computer memory and CPU time due to the reduced domain size. Furthermore, the amplitude modulation allows the wave packet to evolve spontaneously into a turbulent spot, which cannot be achieved if the initial instability wave is strictly periodic (Kachanov 1994). From an acoustic viewpoint, tracking an isolated wave packet has the advantage that the linkage between the calculated sound signal and the specific transition stage is apparent. Once the sound generation properties from a single breakdown (burst) are determined, one could make

statistical inferences regarding the sound of a realistic transitional boundary layer where a large collection of spots are present.

This report summarizes work accomplished to date and the major findings. A longer and more complete version is available as a CTR manuscript (Wang *et al.* 1994).

2. Accomplishments

2.1. Numerical simulation of wave packet transition

The specific problem considered involves a strongly modulated T-S wave packet in a low Mach number, zero pressure gradient boundary layer formed on a rigid, flat plate. In the spirit of Lighthill's theory, the acoustic source functions can be approximated by considering an equivalent incompressible flow since the compressibility effect is negligibly weak. The incompressible Navier-Stokes and continuity equations are solved numerically on a staggered grid using a finite difference scheme developed by Le and Moin (1991). The grid spacing is uniform in the streamwise (x_1) and spanwise (x_3) directions, and non-uniform in the wall-normal direction (x_2). Time advancement is of semi-implicit, three-step Runge-Kutta type combined with a fractional step method. The Poisson equation is solved at the final sub-step to satisfy the divergence-free constraint. The numerical scheme is second order accurate in both space and time.

The domain of integration consists of a rectangular box parallel to the flow direction. A no-slip condition is applied on the wall. At the free-stream boundary a normal velocity distribution based on the Blasius solution and zero vorticity are prescribed. In the spanwise direction periodicity is assumed for all dependent variables. A convective boundary condition capable of maintaining the accurate steady (Blasius) velocity profiles (Wang *et al.* 1994) is used at the downstream boundary.

The unsteady wave packet is introduced into the computational domain from the upstream boundary by requiring that

$$\begin{aligned} u_i(x_1=0) = u_i^B(x_2) + Real\Big\{ & \epsilon^{2D} u_i^{2D}(x_2) e^{-i\beta t} \\ & + \frac{1}{2}\epsilon^{3D} u_i^{3D+}(x_2) e^{i[(\alpha \sin\phi)x_3 - \beta t]} \\ & + \frac{1}{2}\epsilon^{3D} u_i^{3D-}(x_2) e^{i[-(\alpha \sin\phi)x_3 - \beta t]} \Big\} e^{-\left(\frac{t-t_0}{\tau}\right)^4} g(x_3) \end{aligned} \qquad (1)$$

where $u_i^B(x_2)$ represents the Blasius solution for a two-dimensional boundary layer. $u_i^{2D}(x_2)$ and $u_i^{3D\pm}(x_2)$ are the least stable eigenmodes and α is the corresponding eigenvalue, obtained by solving the Orr-Sommerfeld and Squire equations for given frequency $\beta = 0.094$ and oblique angle $\phi = \pi/4$. The eigenfunctions are normalized such that the maximum streamwise velocity has unit magnitude. The disturbance amplitudes are $\epsilon^{2D} = 0.025$ and $\epsilon^{3D} = 0.01$. The streamwise shape of the wave packet is determined by $\tau = 40$ and $t_0 = 120$ in the time-modulating envelope. In addition, symmetry relative to the spanwise center $x_3 = 0$ is destroyed by the

function $g(x_3) = 1 + 0.1(e^{-\left(\frac{x_3-1.73}{1.73}\right)^2} - e^{-\left(\frac{x_3+1.73}{1.73}\right)^2})$. As pointed out by Corral & Jiménez (1991), spanwise asymmetry accelerates the transition process and renders the simulation more manageable. The Reynolds number defined in terms of δ_0^* is $Re = 1000$, which is equivalent to $Re_x \approx 3.38 \times 10^5$ as measured in terms of distance from the leading edge.

In (1) and the subsequent descriptions, the velocities, spatial coordinates, and time are non-dimensionalized with respect to the free-stream velocity U'_∞, the inflow boundary layer displacement thickness δ_0^*, and δ_0^*/U'_∞, respectively. The thermodynamic variables are non-dimensionalized relative to their constant free-stream values.

Computations start out on a $514 \times 130 \times 66$ grid covering a computational domain defined in $0 \leq x_1 \leq 200$, $0 \leq x_2 \leq 20$ and $-\lambda_{x_3}/2 \leq x_3 \leq \lambda_{x_3}/2$, where $\lambda_{x_3} \approx 25.95$ is the spanwise wavelength for the oblique eigenmode pair. As simulation proceeds, resolution requirement becomes increasingly severe within the traveling disturbance region, whereas near the upstream boundary the flow becomes basically steady. Grid refinement is performed twice in conjunction with shifts in computational boundaries following the movement of the wave packet. A cubic-spline interpolation scheme is used to interpolate solutions onto new grids. By the end of the simulation, the computational grid consists of $1282 \times 130 \times 258$ points covering a shortened region $70 \leq x_1 \leq 210$. The entire simulation utilizes approximately 60 single processor CPU hours on CRAY-YMP-C90.

Figs. 1a-f depict a time sequence of the instantaneous contours of the negative spanwise vorticity $-\omega_{x_3}$, which is closely related to the normal shear $\partial u_1/\partial x_2$, at $x_3 \approx 1.1$. Solid lines denote positive contour values, and dashed lines denote negative ones. The plane $x_3 \approx 1.1$, which lies slightly off the spanwise center, is chosen because it corresponds to the approximate location of maximum shear. Notice that due to the slight asymmetry of the initial T-S wave packet, the peak-valley splitting along the spanwise direction during the secondary instability is not as clear-cut as for symmetric disturbances. Nonetheless, the transition is seen to follow closely the route that leads to fundamental (K-type) breakdown.

The complete wave packet enters the upstream boundary $x_1 = 0$ at $t \approx 185$. Through the action of primary and secondary instability mechanisms, it amplifies rapidly, evolving into a detached high shear layer as shown in Fig. 1a. Underneath the shear layer lie a pair of counter-rotating streamwise vortices (lambda vortex) whose structure will be shown later. The high shear layer intensifies to create a kink in Fig. 1b, which breaks down in Fig. 1c to form an eddy (presumably hairpin eddy) while a second kink develops. In Figs. 1d–1f the detached high shear layer continues to disintegrate, shedding eddies into the free stream. In the meantime, vortical activity intensifies in the near wall region, and a new generation of shear layers originates there. The new shear layers are expected to experience similar breakdown processes, known as turbulent "bursts". The flow field depicted in Fig. 1f already bears certain resemblance to turbulence. However, large scale high shear layers and streamwise vortices still dominate the overall flow structure, particularly in the rear part of the wave packet and away from the spanwise center.

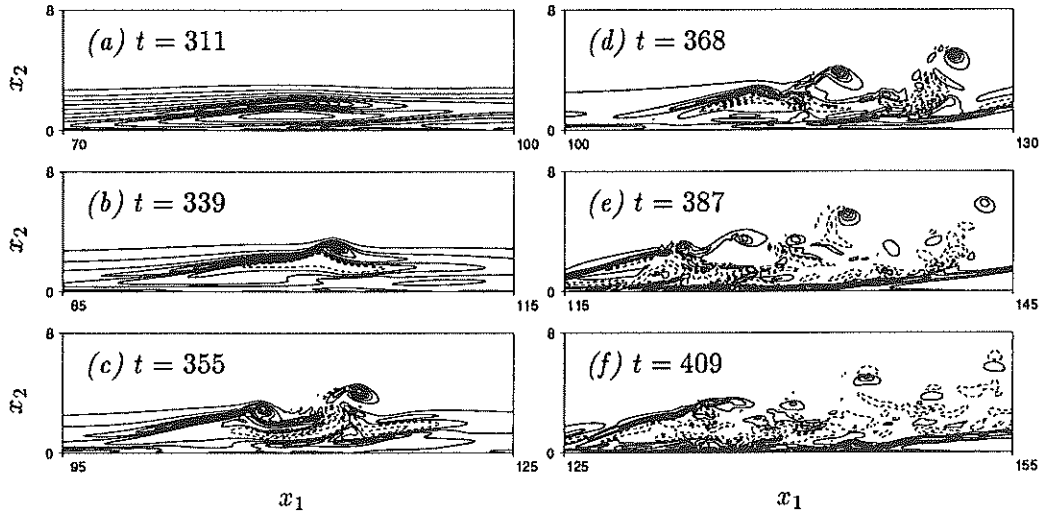

FIGURE 1. Contours of negative spanwise vorticity $-\omega_{x_3}$ at $x_3 \approx 1.1$ during laminar breakdown. Contour values: (a) 0 to 0.94, (b) −0.23 to 1.81, (c) −0.59 to 1.61, (d) −1.30 to 2.13, (e) −1.52 to 3.22, (f) −0.98 to 3.83.

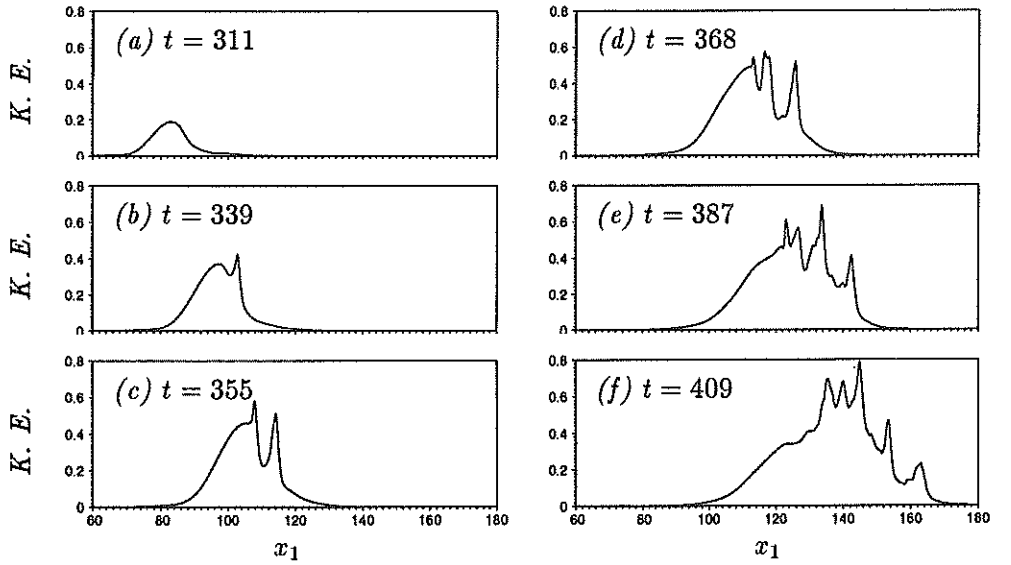

FIGURE 2. Evolution of disturbance kinetic energy integrated over the x_2–x_3 plane during laminar breakdown.

Figs. 2a-f illustrate the streamwise distribution of the disturbance kinetic energy integrated over the x_2–x_3 plane, at time instants corresponding to those in Figs. 1a-f. The energy is calculated based on the excess velocities relative to the steady solution. The snapshots show the nonlinear distortion of the energy waveform which leads to

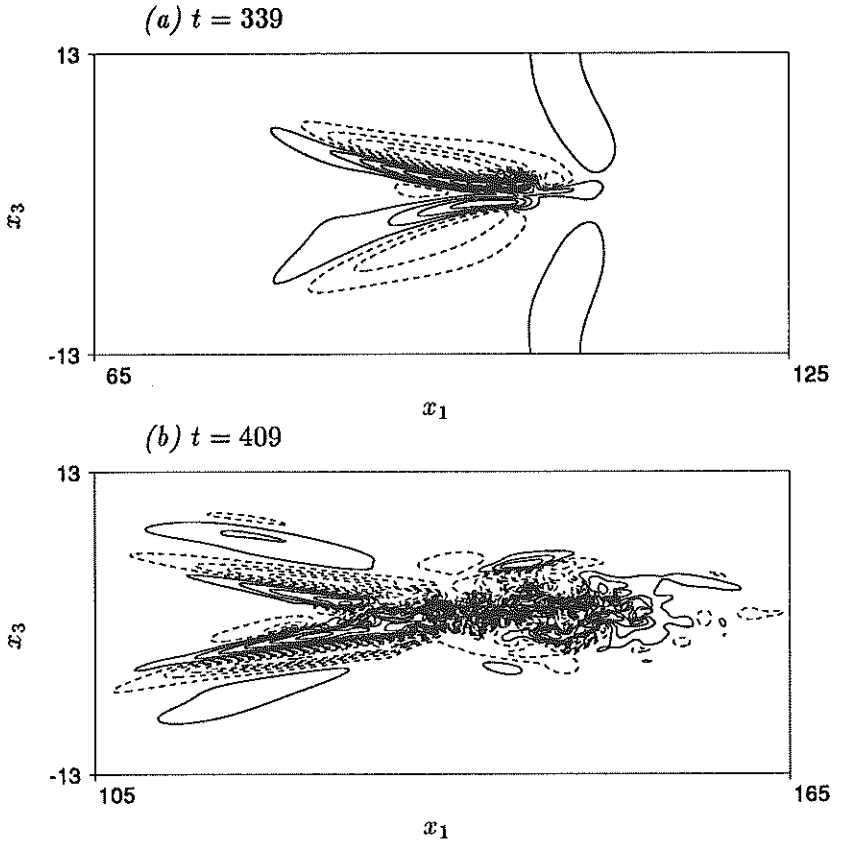

FIGURE 3. Contours of instantaneous normal velocity at $x_2 \approx 1.1$. (a) $t = 339$, contour spacing $= 0.015$; (b) $t = 409$, contour spacing $= 0.02$.

the formation of one, two, and multiple spikes, each corresponding to an eddy. These spikes are observed in experiments for the K-regime breakdown (Kachanov 1994) as high frequency flashes of disturbances on the streamwise-velocity oscilloscope traces. Kachanov notes that the velocity flashes do not disperse while they propagate downstream near the edge of the boundary layer, a feature identifiable with solitons. It is conceivable that the kinetic energy waveforms exhibited in Figs. 2a-f may be modeled by certain evolutionary equations within the framework of soliton theory. The spread of the nonlinear wave packet in the streamwise direction during laminar breakdown is apparent in Figs. 2a-f. The amplitude increase observed in the energy waveform reflects not only the growth in disturbance velocities, but also the spread of the wave packet in the spanwise direction.

In Figs. 3a-b the normal velocity contours in the plane $x_2 \approx 1.1$ are plotted for two time instants before and after laminar breakdown. Fig. 3a shows the two legs of the lambda vortex which merge gradually along the streamwise direction. The lambda vortex is "crippled" in the sense that it has unequal strength in the two legs, caused by the spanwise asymmetry prescribed in the initial disturbance. The

imbalance causes the two legs to become twisted near the tip of the vortex loop, accelerating the breakdown of the streamwise vortex structure and the high shear layer supported by it. This effect can be seen more clearly if one plots streamwise vorticity contours at certain x_2–x_3 cross-sections. Similar observation has been made by Corral & Jiménez (1991). By the time depicted in Fig. 3b, the front portion of the primary lambda vortex has disintegrated, and regions of smaller streamwise vortices emerge. The disturbance region has been elongated since the turbulence-like small-scale structures travel at a faster speed than the lambda vortex. At the rear the lambda vortex legs are still recognizable. Fig. 3b also demonstrates that up to this stage, the disturbance region remains small in the spanwise direction relative to the width of the computational box. Interaction between the neighboring patches is negligible despite the periodicity imposed in the spanwise direction. Thus, the wave packet can be justifiably considered isolated.

The transition scenario described in this section is in qualitative agreement with experimental observations (Gaster 1993; Borodulin & Kachanov 1992). In particular, the coherent structures depicted in Figs. 1e and 1f are remarkably similar to the experimental measurements illustrated in Fig. 31 of Kachanov (1994). Quantitative comparisons are difficult because of disparity in parametric conditions. The results of the present simulation are also in keeping with those of earlier numerical studies (Zang & Hussaini 1990; Kleiser & Zang 1991, for example). The latter are based on a temporal formulation (assuming streamwise periodicity) and do not exceed the two-spike stage. The observed similarity between the two types of simulations confirms that as first suggested by Kachanov (1994), the laminar breakdown of a modulated wave packet proceeds in nearly the same way as that for a periodic T-S wave series. This illustrates the localized nature of resonant mechanisms that lead to laminar breakdown.

2.2. Computation of acoustic radiation

Acoustic computation based on Lighthill's theory is particularly simplified for a compact flow region. In this case the small retarded time effect can be approximated in the sense of multipole source expansions. Based on the integral results of Curle (1955) and Powell (1960), the far-field acoustic pressure can be shown to have the following asymptotic property as $M \to 0$; $|\vec{X}| \to \infty$:

$$\begin{aligned}\frac{4\pi}{\gamma}\left[p(\vec{X},t)-1\right] \approx\ & 2M^4\,\frac{X_\alpha}{|\vec{X}|^2}\dot{R}_\alpha\left(t-|\vec{X}|\right)\\ &+\ M^5\,\frac{X_iX_j+X_i^*X_j^*}{|\vec{X}|^3}\ddot{Q}_{ij}\left(t-|\vec{X}|\right)\\ &+\ 2M^5\,\frac{X_\alpha X_\beta}{|\vec{X}|^3}\ddot{S}_{\alpha\beta}\left(t-|\vec{X}|\right)\end{aligned} \tag{2}$$

where M is the free-stream Mach number and $\vec{X} = M\vec{x}$ is the rescaled far-field position vector, whose image in the rigid wall $X_2 = 0$ is $\vec{X}^* = (X_1, -X_2, X_3)$. Repeated

indices i and j represent summation over 1 to 3, whereas α and β are summed over 1 and 3 only. The three terms on the right side of (2) represent contributions from, respectively, net surface dipoles due to fluctuating wall shear stresses, net volume quadrupoles (including wall reflection) dominated by fluctuating Reynolds stresses, and net surface quadrupoles due to finite spatial distribution of wall shear stresses. The dipole and quadrupole source strengths are determined by

$$\dot{R}_\alpha(t) = \frac{\partial}{\partial t}\int_{A_0} \tau_{\alpha 2}(\vec{y},t)dA(\vec{y}), \tag{3}$$

$$\ddot{Q}_{ij}(t) = \frac{\partial^2}{\partial t^2}\int_{V_0} T_{ij}(\vec{y},t)dV(\vec{y}), \tag{4}$$

$$\ddot{S}_{\alpha\beta}(t) = \frac{\partial^2}{\partial t^2}\int_{A_0} y_\beta \tau_{\alpha 2}(\vec{y},t)dA(\vec{y}), \tag{5}$$

where the Lighthill stress tensor and the viscous stress tensor take the approximate values

$$T_{ij} \approx u_i u_j, \qquad \tau_{ij} \approx \frac{1}{Re}\left(\frac{\partial u_i}{\partial x_j} + \frac{\partial u_j}{\partial x_i}\right), \tag{6}$$

given the small Mach number assumption. The volume integrations are taken over the entire unsteady flow region, and the surface integrals are evaluated on the wall.

A serious difficulty confronts computational acousticians when vortical structures enter or pass out of the computational domain, causing powerful dipole radiation which may mask the true physical sound (Crighton 1993; Wang 1993). This arises because, if the complete disturbance region is not included in the finite computational domain, the time variations of the volume (surface) integrated Q_{ij}, R_α, and $S_{\alpha\beta}$ (cf. (3)–(5)) tend to be dominated by the fluxes of their respective integrand across the integration boundaries rather than by the internal generation of these quantities within the control volume.

Steps have been taken in order to eliminate the non-physical boundary effects. First, the computational boundaries for Navier-Stokes simulation of the source field are maintained sufficiently far away from the region of significant disturbances, as is evident from a comparison of the computational box size ($140 \times 20 \times 25.95$) with the size of flow structures displayed in Figs. 1–3 (note that only part of the domain is plotted to magnify the main feature). This measure alone removes most of the boundary artifacts at the expense of increased computational cost. However, it is impossible to prevent small disturbances from reaching the downstream boundary even if a very long computational domain is used. The difficulty is illustrated in Fig. 4, which depicts contours of the instantaneous normal vorticity at $x_2 \approx 2.3$, $t = 292$. The primary structure at left is identified with the wave packet. The transient ripples induced by the wave packet extend all the way to the right because they are convected near the edge of the boundary layer at a faster speed.

The residual boundary artifacts caused by these ripples are removed by using the corrected quadrupole sources defined as

$$\ddot{Q}'_{ij} = \ddot{Q}_{ij} + \dot{F}_{ij}, \qquad \dot{F}_{ij} = \frac{\partial}{\partial t}\int_S u_1^B T_{ij} dS, \tag{7}$$

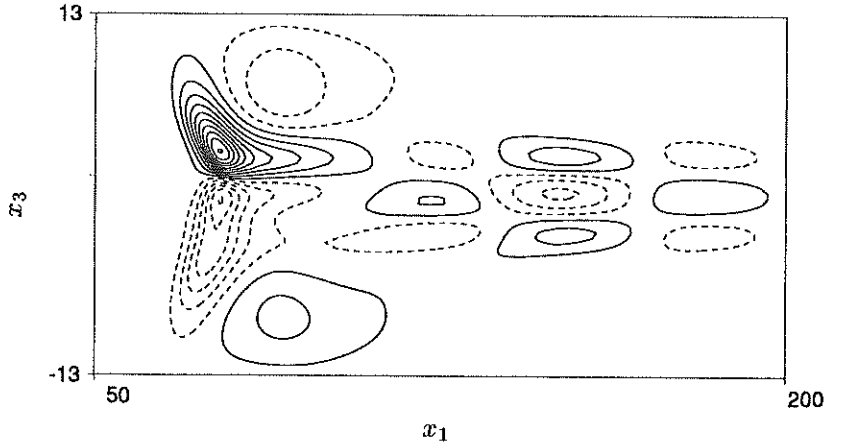

FIGURE 4. Contours of instantaneous normal vorticity at $x_2 \approx 2.3$, $t = 292$. Contour spacing = 0.0015.

where F_{ij} represents the flux of Lighthill stress components at the outflow boundary. Eq. (7) is derived based on a control-volume balance for T_{ij}, recognizing that the physical sound sources are associated only with the Lighthill stresses (predominantly Reynolds stresses) generated internally through nonlinear interactions. Eq. (7) is exact except for the evaluation of the surface flux F_{ij}, which assumes that T_{ij} is convected passively out of the outflow boundary at the local mean velocity. The approximation works well for the present problem, as demonstrated below, because the ripple disturbances are linear and travel at approximately the free-stream velocity. In general, however, the T_{ij} associated with large vortical structures involves nonlinear effects and travels at a phase velocity which is not known *a priori*. More accurate methods for estimating F_{ij} need to be developed, perhaps along the line of Fedorchenko (1986).

Fig. 5 illustrates the effect of flux correction for $\ddot{Q}_{12}$, the component with the largest boundary artifact. The dashed and dotted lines, representing the original quadrupole source and the time-derivative of the outflow boundary flux, respectively, show oscillations of similar magnitude but opposite phase for $t \leq 330$. As a result the corrected acoustic source (the solid line) remains nearly zero during this period. Had the spurious boundary contribution not been subtracted, one would predict incorrectly sound radiation when the wave packet transition is still in an early stage (cf. Figs. 1a-f). At later times, Fig. 5 shows that the boundary flux contribution continues to be significant although the physical source gradually becomes dominant. The vertical dotted line in the figure indicates the time when the computational domain is moved from $0 \leq x_1 \leq 200$ to $40 \leq x_1 \leq 180$. This causes a discontinuity in $\ddot{Q}_{12}$ and $\dot{F}_{12}$, but $\ddot{Q}'_{12}$ remains continuous since the physical source is completely contained within both domains.

In what follows the prime in $\ddot{Q}'_{ij}$ is dropped to simplify notation, with the understanding that the quadrupole sources presented are free of boundary artifacts. Convergence of the quadrupole and dipole source terms is monitored by evaluating

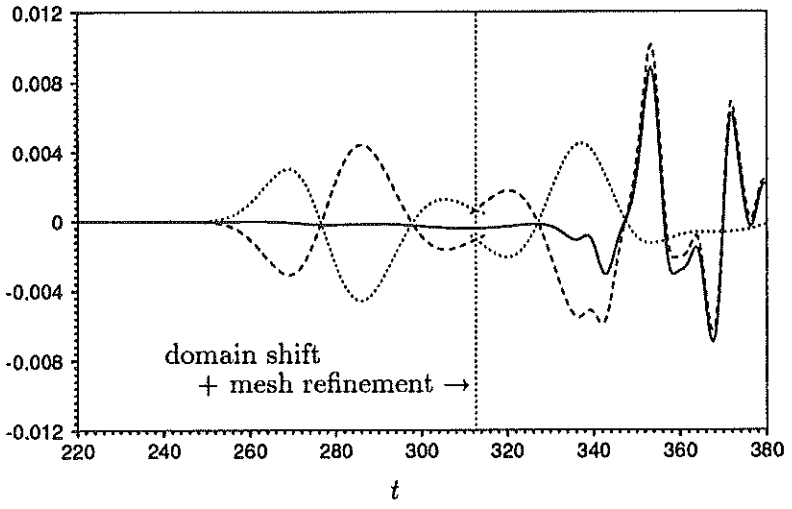

FIGURE 5. Time variation of a quadrupole source component, with and without correction for outflow boundary effect. ---- $\ddot{Q}_{12}$; ····· $\dot{F}_{12}$; —— $\ddot{Q}_{12} + \dot{F}_{12}$.

them in two domains of integration whose downstream boundaries are a short distance (~ 5) apart. Agreement between the two solutions indicates that no boundary effect is present. When the two solutions start to deviate, the computational box is moved to a new downstream location.

2.3. Results and discussion

Figs. 6 illustrate the time-variations of the volume quadrupole source terms $\ddot{Q}_{ij}$ calculated from (4) with appropriate boundary flux corrections. The upper figure depicts the three longitudinal components, and the lower figure depicts the lateral ones. Since the Lighthill stress tensor is symmetric, only six components are needed to define $\ddot{Q}_{ij}$ completely. The characteristics of source oscillations should be analyzed in conjunction with the flow structures shown in Figs. 1a-f. The quadrupole source signals generated by wave packet evolution are relatively weak initially, and then amplify dramatically as the shear layer begins to breaks down. Thereafter, the $\ddot{Q}_{ij}$ curves are seen to develop oscillations dominated by frequencies 5 to 7 times the basic T-S wave frequency (T-S wave period ≈ 66.5).

A close examination of the $\ddot{Q}_{11}$ curve and Figs. 1–2 indicates a strong correlation between source oscillation and vortex-shedding in the boundary layer. At $t = 409$, the number of spikes (eddies) shown in Figs. 2a-f is approximately equal to the number of cycles experienced by $\ddot{Q}_{11}$. Thus it appears that the dominant mechanism for generating quadrupole sound is the intermittent vortex shedding, or bursting, resulting from strong inflexional instability of the high shear layer. This is not unexpected since turbulent stress production occurs mainly during the bursts (Landahl 1975). In his experiments concerning instability of modulated T-S wave trains, Gaster (1993) observes a characteristic bursting frequency of 5 to 6 times the T-S wave frequency, coinciding with the dominant source frequencies

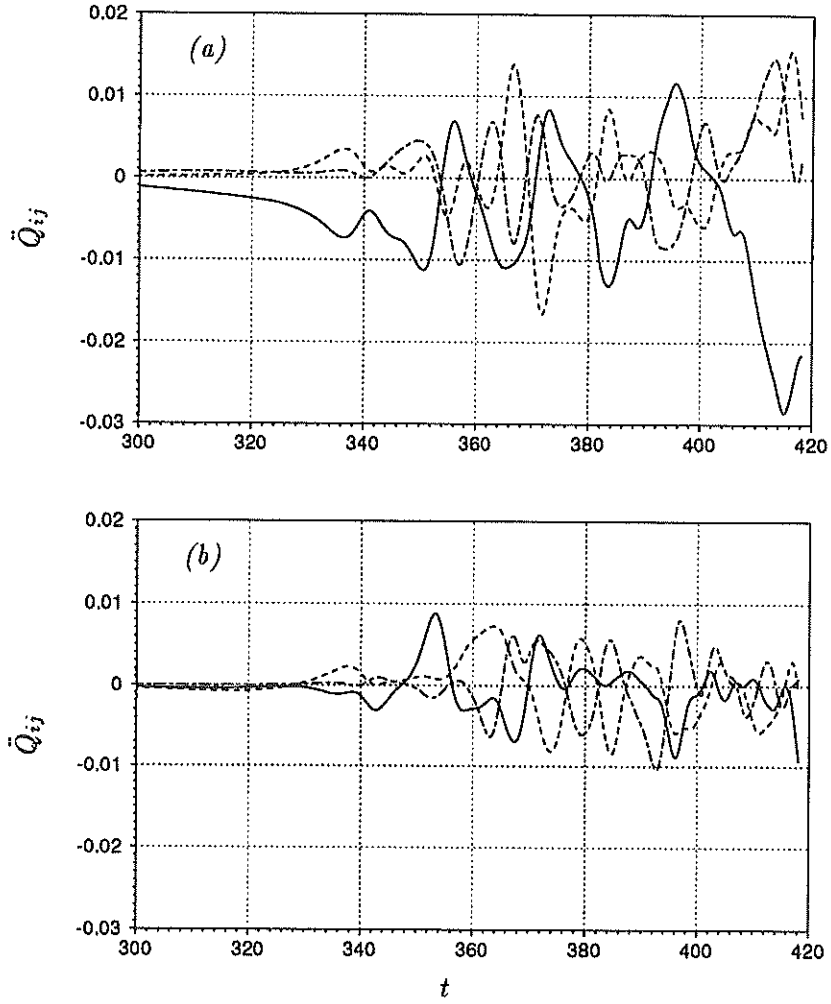

FIGURE 6. Time variations of volume quadrupole sources due to Reynolds stress fluctuation during local laminar breakdown. (a) Longitudinal components: —— $\ddot{Q}_{11}$; ---- $\ddot{Q}_{22}$; —·— $\ddot{Q}_{33}$. (b) Lateral components: —— $\ddot{Q}_{12}$; ---- $\ddot{Q}_{13}$; — — $\ddot{Q}_{23}$.

calculated in the present study. Gaster further notes that the bursting frequency is independent of the Reynolds number. The agreement between the bursting and acoustic source frequencies supports the assertion that the large-scale shear layer instability is primarily responsible for the calculated quadrupole sound.

It is interesting to notice that no significant increase in higher frequency contents is observed in Figs. 6a-b as transition proceeds to create increasingly refined scales. Likewise, the amplitudes for $\ddot{Q}_{ij}$ remain basically invariant with time, even though the total kinetic energy of the source region (the area under each curve in Figs. 2a-f)

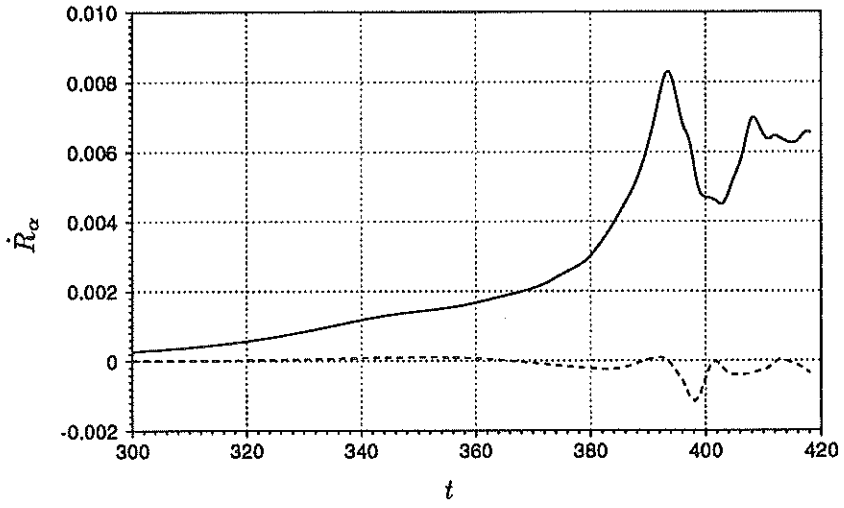

FIGURE 7. Time variations of surface dipole source terms due to viscous wall stress during local laminar breakdown. —— $\dot{R}_1$; ---- $\dot{R}_3$.

grows at an exponential rate. These observations can be explained in terms of the localized nature of bursting which dominates the instantaneous sound production. The small-scale features and the convected large eddies produced during previous bursts are less efficient as quadrupole acoustic sources, although they contain large amount of disturbance energy.

In Fig. 7 the two net acoustic dipoles caused by fluctuations of wall shear stress exerted on the fluid are plotted. They are dominated by low (T-S wave) frequency, small amplitude phenomena during the process of shear layer lift-up and the first three bursts. Figs. 1a-f show clearly that within this period, the near-wall region is little affected by the violent events outside. As the laminar wave packet approaches the turbulent spot stage, the near-wall shear intensifies, giving rise to a surge in higher frequency dipole strength. The magnitudes of $\dot{R}_3$ in Fig. 7, as well as $\ddot{Q}_{13}$ and $\ddot{Q}_{23}$ in Figs. 6a-b, reflect the extent of spanwise asymmetry during flow development. They would vanish if symmetry conditions were imposed for the simulation.

The surface quadrupole acoustic sources given by (5) are caused by the changing spatial distribution of wall shear stress. They represent an $O(M)$ correction to the wall-stress induced dipole radiation in the compact source limit. Like the dipole source terms, the surface quadrupole components are small until the inner boundary layer is excited at a late laminar breakdown stage as illustrated in Fig. 8. The segments of $\ddot{S}_{\alpha\beta}$ plotted have magnitudes comparable with those of the volume quadrupoles depicted in Figs. 6a-b, but at higher frequency. Before $t = 390$, however, contribution from $\ddot{S}_{ij}$ is insignificant.

Figs. 6–8 demonstrate that the acoustic emission level is very low at early stages of wave packet transition. At the earliest instant plotted ($t = 300$), the wave packet has already evolved into a lambda vortex-high shear layer structure. Prior to that, the acoustic source terms exhibit either monotonic growth or extremely low amplitude

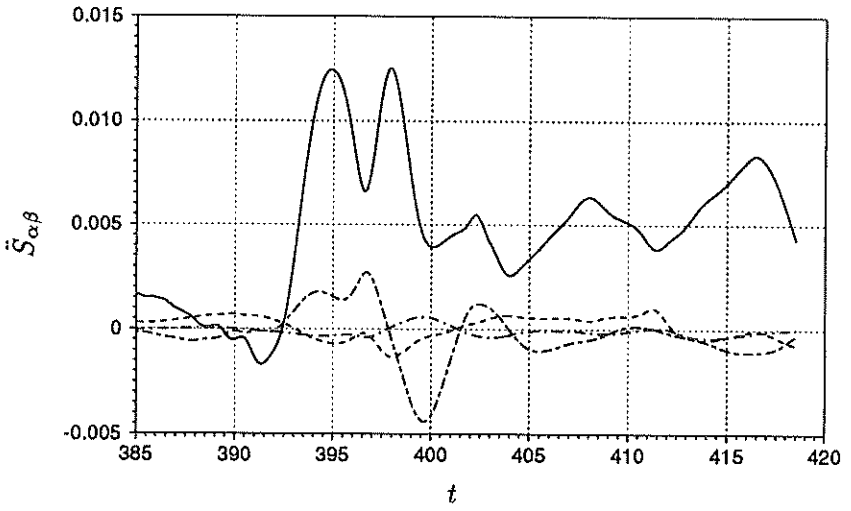

FIGURE 8. Time variations of surface quadrupole sources due to viscous wall stress during local laminar breakdown. —— $\ddot{S}_{11}$; ---- $\ddot{S}_{13}$; — — $\ddot{S}_{31}$; —·— $\ddot{S}_{33}$.

oscillations at the basic T-S wave frequency. Thus it can be concluded that linear and weakly nonlinear amplification of the T-S wave packet produces insignificant sound relative to the more violent bursting process later. Unfortunately, only the former regime is amenable to rigorous analytical treatment (*e.g.*, Ffowcs-Williams 1967; Akylas & Toplosky 1986; Haj-Hariri & Akylas 1986).

For flow-noise problems it is generally recognized that the energy-containing coherent structure provides the predominant noise source. The fine-scale structure associated with high frequency phenomenon is largely irrelevant (Crighton 1975), a conclusion supported by the lack of relatively high frequency components in Figs. 6–8. To test the sensitivity of quadrupole sources to the size of flow structure, the computed flow field is filtered in the x_1–x_3 plane using a box filter of varying width before the volume integration in (4) is performed. The results for $\Delta_i = 2\Delta x_i$, $4\Delta x_i$, and $8\Delta x_i$, where Δ_i is the filter width in the ith direction and Δx_i is the mesh spacing, are compared in Fig. 9 with those without filtering. For brevity only the three longitudinal components are given; the three lateral ones behave in the same way. Clearly, the basic source characteristics are preserved after filtering the flow field with a filter of widths up to $4\Delta_i$ ($2\Delta_i$ for $\ddot{Q}_{22}$). With a filter width of $8\Delta_i$, the results are still in qualitative agreement with their unfiltered counterparts in terms of basic frequency and amplitude. This verifies that removing small-scale flow structures indeed has little impact on the distant-field sound radiation. Since the application of a box filter also alters the lower wavenumber (large-scale) components to some extent, the actual agreement between unfiltered and filtered source quantities might be even better had the large-scale motion been truthfully preserved.

The comparison made in Fig. 9 is also an indication of numerical convergence. It illustrates that the direct numerical simulation for the source field has adequately

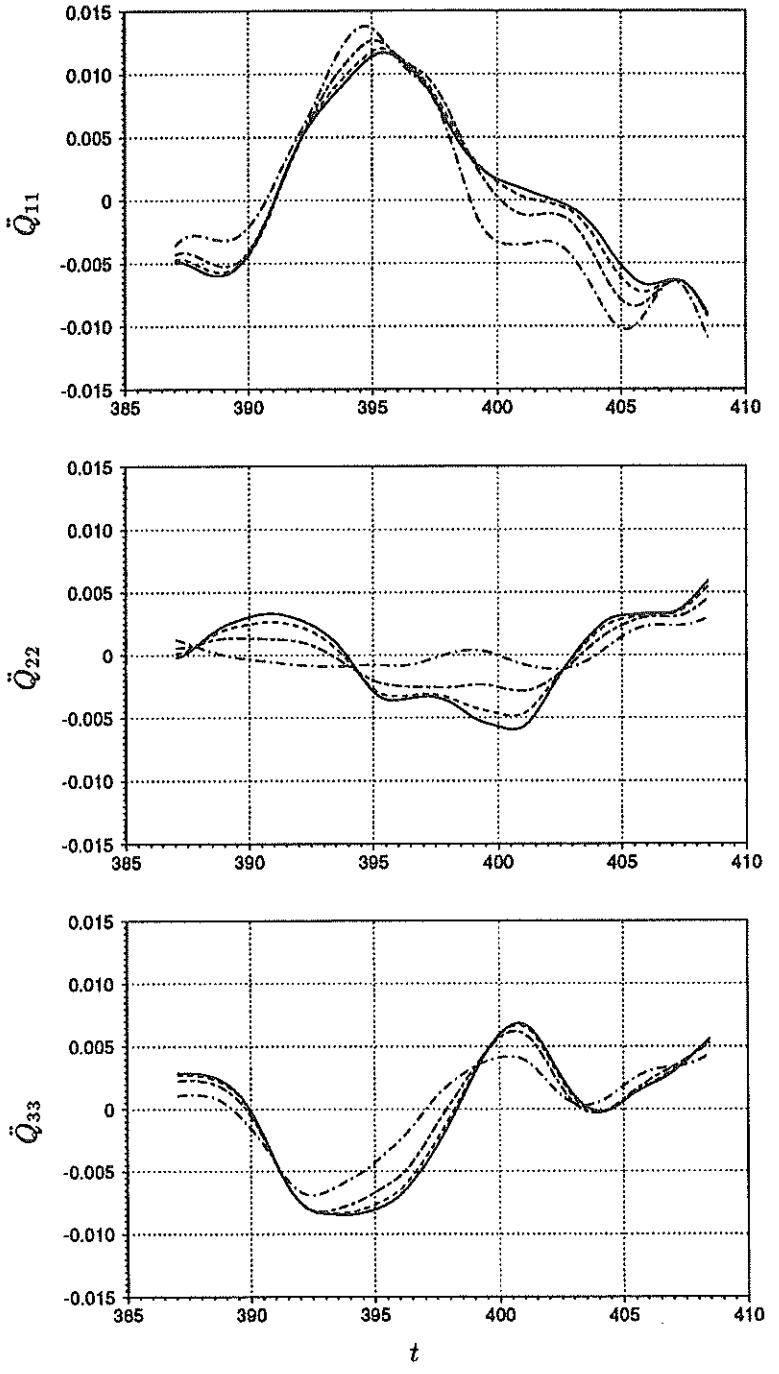

FIGURE 9. Longitudinal quadrupole sources calculated based on the velocity field filtered in the x_1–x_3 plane with filter width Δ_i. ——— no filtering; - - - - $\Delta_i = 2\Delta x_i$; — — — $\Delta_i = 4\Delta x_i$; —·— $\Delta_i = 8\Delta x_i$.

resolved the scales relevant to sound production. In fact, the simulation can be conducted on a coarser grid if the subgrid-scale stress can be modeled adequately. This suggests the promising role that can be played by the less expensive large-eddy simulation methods for flow-noise prediction.

An issue worthy of particular attention is the relative importance of wall-shear-stress radiation *vs.* volume Reynolds stress radiation. Eq. (2) and the numerical results in Figs. 6 and 7 indicate that at the late laminar breakdown stage, viscous dipole radiation is important or even dominant for low Mach number flows, in agreement with Landahl (1975) but at variance with conclusions of Howe (1979) and Haj-Hariri & Akylas (1985), who assert that surface stress contribution is in general negligible. The contradiction may arise because Howe's (1979) analysis is limited only to the low wavenumber (acoustic) components of the wavenumber-frequency spectrum, whereas the analysis of Haj-Hariri & Akylas (1985) fails to utilize the pertinent turbulence scales in estimating the Lighthill source terms at high Reynolds number. Furthermore, the three aforementioned studies are all concerned with fully turbulent boundary layers, although Landahl (1975) notes the qualitative similarities between the high shear layer breakdown during transition and the turbulent bursting in the inner layer of a turbulent boundary layer.

As an example, Figs 10a and 10b compare the distant sound field generated by, respectively, the inviscid Reynolds stress (volume quadrupoles) and viscous wall-stress (sum of surface dipoles and quadrupoles), in terms of iso-contours of the acoustic pressure $\hat{p}$ $(= p - 1))$ at $X_3 = 0$ and $t = 420$. The source region is centered at $\vec{X} = 0$, bearing in mind that $\vec{X}$ is scaled relative to the acoustic length scale. The free-stream Mach number is $M = 0.02$, characteristic of underwater applications. At the time instant plotted, the shear-stress induced sound is mainly confined in a region close to the source (the latest signal depicted at $|\vec{X}| = 10$ is emitted at $t = 410$). The quadrupole radiation pattern suggests contributions from the longitudinal components, but not the lateral ones. The latter are identically zero due to both cancellations from wall reflection and the specific plane $(X_3 = 0)$ selected for plotting (cf. (2)). Given the extremely low Mach number, the total radiated field obtained by summing the results in Figs. 10a and 10b is dominated by the surface stress contribution, as is evident from Fig. 10c. The relative effect of volume quadrupoles is, of course, also dependent on the orientation of the plotting plane. For instance, quadrupole radiation is felt more strongly in the $X_1 = 0$ plane than in the plane plotted. When the Mach number is increased to $M = 0.1$, the volume quadrupole sound is found to be comparable in strength with that due to wall-shear-stress, particularly in the plane $X_1 = 0$.

3. Conclusions and future directions

A computational study has been carried out concerning the sound emission from a localized disturbance as it undergoes transition to turbulence in a boundary layer formed on a flat, rigid surface. The flow is characterized by small free-stream Mach number and a Reynolds number of 1000 based on the displacement thickness. Direct numerical simulation is applied in conjunction with the Lighthill acoustic analogy

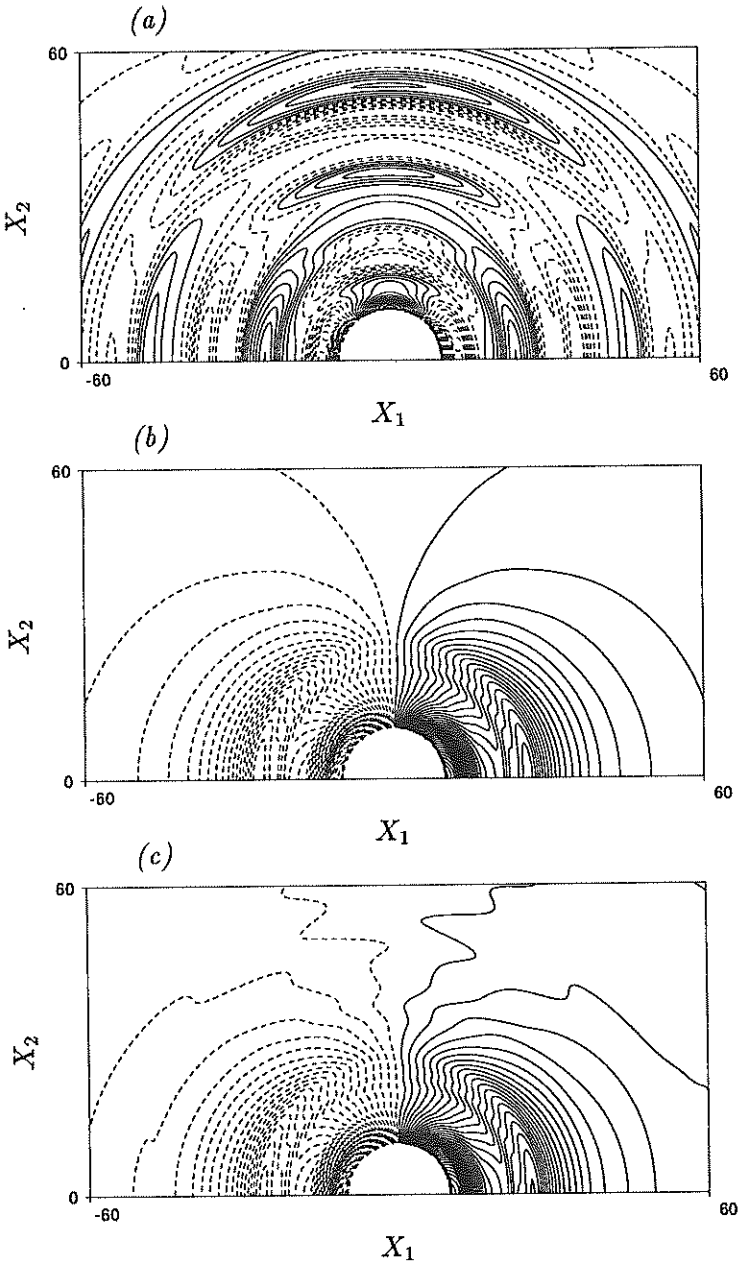

FIGURE 10. Iso-contours of the far-field acoustic pressure in the plane $X_3 = 0$ at $t = 420$, radiated during laminar breakdown of an isolated wave packet. The free-stream Mach number $M = 0.02$. (a) Volume Reynolds stress contribution (contour levels from -1.02×10^{-12} to 0.50×10^{-12}); (b) wall shear-stress contribution (contour levels from -2.25×10^{-11} to 2.31×10^{-11}); (c) total acoustic pressure (contour levels from -2.31×10^{-11} to 2.19×10^{-11}).

to determine the near-field flow dynamics and the far-field sound, respectively. The objectives are to establish a relationship between specific flow processes and the emitted acoustic signals, and to identify the primary noise source.

The boundary-layer disturbance initially consists of a modulated, three-dimensional T-S wave packet emulating that excited by free-stream turbulence in natural transition. Detailed accounts of the subsequent evolution, from the early linear stage to the final laminar breakdown, are obtained by solving the full incompressible Navier-Stokes equations. The simulation allows streamwise growth of the boundary layer thickness as well as spanwise asymmetry. The latter effect promotes interaction between the (unequal) lambda vortex legs and accelerates the high shear layer breakdown and the associated eddy shedding. The route to turbulence is seen to follow the usual sequence of events for the fundamental breakdown type. The flow structures are in qualitative agreement with the experimental observations of Borodulin and Kachanov (1992).

Acoustic computation based on the Lighthill theory is facilitated by a multipole Taylor series expansion in the compact source limit. The radiated far-field acoustic density (pressure) comprises of, to $O(M^5)$ relative to the mean, contributions from net surface dipoles caused by viscous wall shear stresses, net volume quadrupoles due to fluctuating Reynolds stresses, and net surface quadrupoles due to finite spatial distribution of wall shear stresses. All the sources produce negligible sound throughout the primary and secondary instability processes of the wave packet. As the detached high shear layer starts to disintegrate, dramatical amplification occurs for the volume quadrupole sound. The primary frequency (5–7 times the basic T-S wave frequency) of quadrupole radiation corresponds to the frequency of hairpin eddy (spike) generation in the near-field, indicating the latter to be the physical source. The surface dipole and quadrupole sources experience a surge in strength at a later breakdown stage caused by the activation of the high-shear wall layer as the disturbance region evolves to a turbulence spot.

This study suggests that for boundary layer transition at low Mach number, the fluctuation in viscous wall stress takes a significant part in radiating sound to the surrounding. It is in fact the primary sound source at later laminar breakdown stages.

An interesting extension of the present work would be to explore the suitability of large-eddy simulation (LES) techniques for simulating the laminar boundary layer breakdown process and calculating the acoustic source terms. LES possesses tremendous potential in terms of reducing the computational cost drastically while still capturing the energy-containing unsteady flow features essential to noise generation. An earlier study by Piomelli *et al.* (1990) suggests that the Smagorinsky subgrid-scale (SGS) model is excessively dissipative, resulting in less intense high shear layers and delayed transition. New SGS models developed at CTR, such as the dynamic SGS model (Germano *et al.* 1991), offer improved prospects for predicting the important transitional flow structures accurately.

A separate project commenced recently concerns noise radiation caused by turbulent flow past a hydrofoil/airfoil. Broadband noise is known to exist when turbulent

boundary layers interact with a sharp trailing edge as a result of hydrodynamic pressure scattering. In addition, high angles of attack and blunt trailing edges cause flow separation and vortex shedding, which are the source of distinct peaks in the noise spectra (Brooks & Hodgson 1981). A numerical noise-prediction method will be developed using LES in conjunction with aeroacoustic theories. The turbulent boundary layer and near-wake flows are simulated using LES, and the radiated far-field sound is calculated within the framework of the Lighthill theory, taking advantage of experiences gained through the present project. The prediction method can be validated by comparing the numerical results with the experimental data of Brooks & Hodgson (1981).

Acknowledgements

This work was produced in collaboration with Prof. S. K. Lele and Prof. P. Moin. We wish to thank Dr. K. Shariff and Mr. B. Mitchell for fruitful discussions during the course of this work. Appreciation is extended to Mr. Y. Na for providing the original Navier-Stokes code and related assistance, and to Mr. S. Collis for providing the Orr-Sommerfeld eigensolver. Computations were carried out on the NAS facilities at NASA Ames Research Center. This project was supported in part by the Office of Naval Research.

REFERENCES

AKYLAS, T. R. & TOPLOSKY, N. 1986 The sound field of a Tollmien-Schlichting wave. *Phys. Fluids.* **29,** 685–689.

BORODULIN, V. I. & KACHANOV, Y. S. 1992 Experimental study of soliton-like coherent structures. In *Eddy Structure Identification in Free Turbulent Shear Flows.* IUTAM Symposium, Poitiers, 1992.

BROOKS, T. F. & HODGSON, T. H. 1981 Trailing edge noise prediction from measured surface pressures. *J. Sound & Vib.* **78,** 69–117.

CORRAL, R. & JIMÉNEZ, J 1991 *Direct Numerical Simulation of the Leading Edge Boundary Layer*, Technical Note ETSIA/MF-916, Dept. of Fluid Mech., Universidad Politécnica Madrid.

CRIGHTON, D. G. 1975 Basic principles of aerodynamic noise generation. *Prog. Aerospace Sci.* **16,** 31–96.

CRIGHTON, D. G. 1993 Computational aeroacoustics for low Mach number flows. In *Computational Aeroacoustics.* ICASE/NASA LaRC Series, (Hardin J. C. and Hussaini, M. Y. Eds.), Springer-Verlag.

CURLE, N. 1955 The influence of solid boundaries upon aerodynamic sound. *Proc. Royal Soc. London Ser. A.* **231,** 505–514.

FARABEE, T. M., HANSEN, R. J., & KELTIE, R. F. (Eds.) 1989 *Flow-Induced Noise Due to Laminar-Turbulence Transition Process,* ASME NCA–Vol. 5, Symposium for ASME Winter Annual Meeting, San Francisco, 1989.

FEDORCHENKO, A. T. 1986 On vortex outflow through the permeable boundary of the computational domain of non-stationary subsonic flow. *U.S.S.R. Comput. Maths. Math. Phys.* **26**, 71–80.

FFOWCS-WILLIAMS, J. E. 1967 Flow noise. In *Underwater Acoustics*, Vol. 2, Chap. 6, Plenum Press.

GASTER, M. 1993 The origins of turbulence. In *New Approaches and Concepts in Turbulence,* Monte Verita Ser. (Dracos, T. A. & Tsinober, A. Eds.), Birkhauser Boston.

GERMANO, M., PIOMELLI, U., MOIN, P. & CABOT, W. H. 1991 A dynamic subgrid-scale eddy viscosity model. *Phys. Fluids A.* **3**, 1760-1765.

HAJ-HARIRI, H. & AKYLAS, T. R. 1985 The wall-shear-stress contribution to boundary-layer noise. *Phys. Fluids.* **28**, 2727–2729.

HAJ-HARIRI, H. & AKYLAS, T. R. 1986 Sound radiation by instability wave packets in a boundary layer. *Stud. Appl. Math.* **75**, 57–76.

HOWE, M. S. 1979 The role of surface shear stress fluctuations in the generation of boundary layer noise. *J. Sound & Vib.* **65**, 159–164.

KACHANOV, Y. S. 1994 Physical mechanisms of laminar-boundary-layer transition. *Ann. Rev. Fluid Mech.* **26**, 411–482.

KLEISER, L. & ZANG, T. A. 1991 Numerical simulations of transition in wall-bounded shear flows. *Ann. Rev. Fluid Mech.* **23**, 495–537.

LANDAHL, M. T. 1975 Wave mechanics of boundary layer turbulence and noise. *J. Acoust. Soc. Am.* **57**, 824–831.

LE, H. & MOIN, P. 1991 An improvement of fractional step methods for the incompressible Navier-Stokes equations. *J. Comput. Phys.* **92**, 369–379.

LIGHTHILL, M. J. 1952 On sound generated aerodynamically; I. General theory. *Proc. Roy. Soc. London Ser. A.* **211**, 564–587.

PIOMELLI, U., ZANG, T. A., SPEZIALE, C. G., & HUSSAINI, M. Y 1990 On the large-eddy simulation of transitional wall-bounded flows. *Phys. Fluids A.* **2**, 257–265.

POWELL A. 1960 Aerodynamic noise and the plane boundary. *J. Acoust Soc. Am.* **32**, 982–990.

WANG, M. 1993 Sound radiation due to boundary layer transition. *Annual Research Briefs–1993* Center for Turbulence Research, NASA Ames/Stanford Univ., 299–312.

WANG, M, LELE, S. K., & MOIN, P. 1994 Sound radiation during local laminar breakdown in a low Mach number boundary layer. *CTR Manuscript No. 153,* NASA Ames/Stanford Univ.

ZANG, T. A. & HUSSAINI, M. Y. 1990 Multiple paths to subharmonic laminar breakdown in a boundary layer. *Phys. Rev. Lett.* **64**, 641–644.